Materials Advances

ROYAL SOCIETY OF CHEMISTRY

PAPER

View Article Online
View Journal | View Issue

Cite this: *Mater. Adv.*, 2026, 7, 2322

Analysis of mechanical properties in lead-free solders subjected to flash aging

Md Nurul Islam, † Ruman Ahmed Shijan, † Mohammad Motalab * and Md. Rafat Al Razy Rafi

Lead-free solder alloys, particularly those based on tin, silver, and copper, have recently become very popular because of their better mechanical and electrical characteristics and environmentally friendly nature compared to lead-based solder alloys. Although previous studies have focused on how aging and doping affect the stress–strain behavior of SAC305 at the macroscale, this study investigates the effects of isothermal flash aging and zinc (Zn) doping on SAC305 at the nanoscale. Using molecular dynamics simulations, the stress–strain behavior of the SAC305 solder alloy with different percentages of Zn doping is analyzed after subjecting the alloys to varying isothermal flash aging conditions. The thermal aging process involves heating from 300 K to 420 K at 5 K ps^{-1}, holding at 420 K for durations ranging from no aging to 5 nanoseconds, and cooling back to 300 K at the same rate. The stress–strain behavior of these materials is examined under tensile loading at a strain rate of 1×10^9 s^{-1}. The results show that mechanical parameters such as the ultimate tensile strength (UTS), Young's modulus (YM), and energy absorption capacity are greatly affected by isothermal aging. Longer aging durations lower the average atomic volume (AV) and produce denser materials, thereby improving the UTS and YM. However, the priority for long-term solder joint reliability is mechanical stability, which is best achieved through minimal changes in these properties over time. Radial distribution function (RDF) fluctuations are observed with aging, showing changes in the atomic structure. Among the Zn doping levels tested, 0.75% Zn proved to be the most effective in minimizing the effects of aging, as it exhibited the lowest RDF fluctuation with aging, along with the least variation in the UTS, YM, and energy absorption capacity, thus providing the best mechanical stability. This study highlights the potential of nanoscale Zn doping as an effective method for enhancing the mechanical reliability of lead-free solder alloys for high-performance and environmentally friendly electronic applications.

Received 9th December 2025,
Accepted 10th January 2026

DOI: 10.1039/d5ma01436k

rsc.li/materials-advances

1. Introduction

The electronics industry is moving towards lead-free soldering because of increasing awareness regarding environmental and public health issues associated with lead exposure.[1] In response to these concerns, various lead-free alternatives have been developed, notably tin-based alloys, such as Sn–Ag and Sn–Ag–Cu (SAC). Their thermal performance and mechanical strength are thoroughly examined to guarantee their reliability.[2–4] These lead-free solders have several advantageous properties, including a comparatively low melting point,[5] strong wettability and solder joint reliability,[6] and improved thermal and mechanical behavior.[7,8] Additionally, they demonstrate good electrical conductivity[9] and compatibility with modern electronic components,[10,11] making them suitable for a wide range of applications. Common applications include flip-chip solder bumping, die attachment, microelectronic packaging, surface mounting (SMT), and through-hole component assembly, such as pin-through-hole (PTH).[12–14]

Despite these advantages, lead-free solders still have some drawbacks. Challenges such as copper dissolution, rapid intermetallic compound (IMC) growth, high production costs, and the formation of tin whiskers remain ongoing concerns in the industry.[15–17] In contrast to lead-free alternatives, Sn–Pb solder is still commonly used because of its low melting temperature, easy spreading, and ability to prevent the transformation of white tin into gray tin.[18] The mechanical behavior of Sn–Pb solders, such as creep and plasticity, has been studied extensively through uniaxial tensile tests conducted under varying annealing conditions, strain rates, and temperatures.[19] Additionally, the tensile behavior of Sn–Pb solders under temperature variations has been compared to that of lead-free solders

Department of Mechanical Engineering, Bangladesh University of Engineering and Technology, Dhaka 1000, Bangladesh. E-mail: mdnurul.buet@gmail.com, rumanahmed.shijan@gmail.com, abdulmotalab@me.buet.ac.bd, rafi80729@gmail.com

† These authors contributed equally.

across different strain rates, revealing critical insights into their mechanical performance.[20]

At elevated temperatures, solder joints undergo gradual microstructural evolution, which significantly affects their mechanical behavior.[21] During thermal aging, prolonged exposure to high temperatures encourages microstructural coarsening by increasing the average size of IMC particles, ultimately leading to the deterioration of material properties.[22] Higher aging temperatures in the case of SAC305 cause IMC to grow more quickly, leading to a coarser microstructure that weakens both the yield strength (YS) and ultimate tensile strength (UTS).[23] Specifically, SAC305 solder joints experience a decline in UTS under isothermal aging conditions, underscoring the detrimental impact of prolonged thermal exposure on mechanical performance.[24] However, the incorporation of doping elements, such as zinc (Zn)[25] and lanthanum (La),[26] has been demonstrated to mitigate these negative effects by delaying IMC growth and preventing the formation of Kirkendall voids. The doping of Zn into Sn–1Ag–0.5Cu significantly alters its microstructure and tensile properties, with optimal performance observed at specific Zn concentrations.[27] This modification effectively reduces the formation of IMCs and helps prevent the development of Kirkendall voids and surface whiskers.[28–30] Furthermore, recent studies[31] have indicated that doping impacts the rate at which intermetallic layers form in Sn–Ag–Cu solder alloys.

Research has explored various strategies to improve the strength and thermal stability of lead-free solder materials. For example, Pang *et al.*[32] utilized finite element analysis to evaluate how heat and loading speed affect solder joint durability. Chowdhury *et al.*[33] studied the behavior of SAC solders with added elements using water-quenched solidification. In addition, atomistic modeling techniques have been employed to observe the microstructural evolution during quenching and to gain deeper insights into the crystallization pathway.[34] Li *et al.*[35] focused on the initial phase formation and grain structure evolution in AlCoCrCuFeNi alloys under different cooling rates, while Zhang *et al.*[36] analyzed the growth of tin whiskers and the evolution of IMCs in SAC307 solder joints through computational methods. Computational studies of SAC alloys with varying Ag contents have provided valuable insights into their thermomechanical properties at different temperatures.[37]

Aging studies on other alloys, such as Al–Cu–Mg, demonstrate that single-stage isothermal aging at varying temperatures can lead to the formation and coarsening of strengthening phases, which directly affect strength and elongation.[38] Similarly, the tensile behavior and high-temperature mechanical performance of lead-free solders have been widely examined to assess the effects of aging and temperature-dependent IMC formation.[39,40]

To the best of our knowledge, no numerical analysis has been conducted at the nanoscale to evaluate the impact of isothermal aging on solder alloys or to identify the optimal amount of specific doping elements to mitigate these isothermal aging effects. In this study, the SAC305 atomistic models were heated to 420 K at a steady rate of 5 K s^{-1}, followed by isothermal aging for various durations. After aging, the models were cooled to room temperature at the same constant cooling rate of 5 K s^{-1}. The cooled samples were subjected to uniaxial tensile testing to analyze changes in the mechanical properties, including UTS, YM, and energy absorption capacity up to UTS. Additionally, the same process was applied with varying Zn doping levels to determine the optimal doping level to mitigate the aging effects. This study employs the modified embedded atomic model (MEAM) potential[41,42] to perform a detailed atomistic analysis.

2. Methodology

The methodology employed in this study is organized into five key components to enable the accurate modeling and analysis of SAC305 and Zn-doped SAC305 alloys. These are as follows: (1) the modified embedded atom method (MEAM) potential for representing interatomic interactions, (2) the hybrid/overlay pair style approach used to overcome the absence of a unified MEAM potential for the multicomponent SAC305 system, (3) atomic structure modeling for constructing and doping alloy models, (4) molecular dynamics (MD) simulation setup and procedures, and (5) the atomic clustering strategy adopted to better represent realistic alloying conditions. Each component is detailed in the subsequent subsections.

2.1 Meam potential

In this study, molecular dynamics simulations were performed using a large-scale atomic/molecular massively parallel simulator (LAMMPS). For effective modeling of atomic interactions, the modified embedded atom method (MEAM) was used, which is an improvement over the conventional embedded atom method (EAM) because it adds angular dependency to the force field. This inclusion enhances the model's accuracy in representing interatomic forces, particularly in numerous complex intermetallic systems.

The MEAM potential calculates the total energy of a system by combining two principal components: embedding energy and pairwise interaction energy. The total energy E of all the atoms in the system can be expressed as follows:[43]

$$E = \sum_i \left\{ F_i(\overline{\rho}_i) + \frac{1}{2}\sum_{i \neq j} \varphi_{ij}(r_{ij}) \right\}, \quad (1)$$

where F_i denotes the embedding energy function, which depends on the background electron density ρ_i at atom i, while $\phi_{ij}(r_{ij})$ represents the pair potential between atom i and its neighboring atom j located at a distance r_{ij}. The summation includes all neighboring atoms within a predefined cutoff radius.

To ensure accurate simulation outcomes, this study relied on MEAM parameters that have already been validated in previous studies. Table 1 lists the parameter values used in the simulations in this study.

Table 1 Selected MEAM parameters for Sn, Ag, Cu, and Zn used in this study[44–49]

Parameters	Sn	Ag	Cu	Zn
E_c (eV)	3.08	2.85	3.54	1.09
r_0 (Å)	3.44	2.92	2.54	2.77
α	5.09	5.89	5.1	7.389
A	1.12	1.06	1.07	0.70
β_0	5.42	4.45	3.63	3.50
β_1	8	2.20	2.20	3.00
β_2	5	6	6	0.00
β_3	6	2.20	2.20	2.00
t_0	1	1	1	1
t_1	3	5.541	3.138	3.00
t_2	5.707	2.45	2.494	6.00
t_3	0.3	1.288	2.95	−10.00

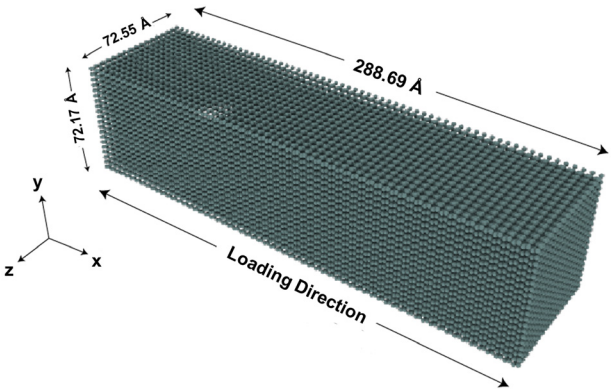

Fig. 1 The atomic model of β-Sn.

2.2 Hybrid/overlay pair style

In this study, the modified embedded atom method (MEAM) potential was used for molecular dynamics simulations. However, a significant challenge arose while working with SAC305 and Zn-doped SAC305 alloys: no comprehensive MEAM potential files, such as SnAgZn.meam or SnAgCuZn.meam, were available in the literature to describe the interactions among Sn, Ag, Cu, and Zn. Consequently, a hybrid/overlay approach was adopted in LAMMPS, in which the individual MEAM potentials for each element were combined to accurately model interatomic interactions. The hybrid/overlay style allows for the superposition of energy contributions from multiple potential definitions; specifically, we used individual optimized MEAM files for each pure element (Sn.meam, Ag.meam, Cu.meam, and Zn.meam) to define the unary (I–I) interactions. Crucially, the binary (I–J) inter-species interactions (*e.g.*, Sn–Ag, Sn–Zn) were not manually defined but were automatically calculated by LAMMPS using the mixing rules inherent to the MEAM potential formalism itself, as enabled by the hybrid/overlay command, ensuring a complete description of the alloy system's interatomic forces. Every element was assigned a unique MEAM potential, and interactions were precisely controlled to avoid unintentional cross-element interactions. The hybrid/overlay method improves the physical correctness of the molecular dynamics simulation, therefore enabling an improved investigation of the mechanical behavior. To the best of our knowledge, this hybrid method has never been used for SAC305 or Zn-doped SAC305; therefore, this work is unique and the first of its kind in the field of lead-free solder simulations.

2.3 Atomic structure modeling

In this study, the initial β-Sn atomic configuration of 81 920 atoms was generated using Atomsk[50] software, with a simulation box sized 288.69 × 72.17 × 72.55 Å^3 (Fig. 1). Five nanostructures of solder alloys were modeled (Fig. 2): (i) SAC305 and SAC305 doped with (ii) 0.25%, (iii) 0.5%, (iv) 0.75%, and (v) 1% Zn. All these alloy compositions were generated based on the weight percentages, consistent with the standard definition of SAC305 and its Zn-doped variants. A Python[51,52] script was then used to convert the target weight percentages of Sn, Ag, Cu, and Zn into the corresponding number of atoms using their atomic

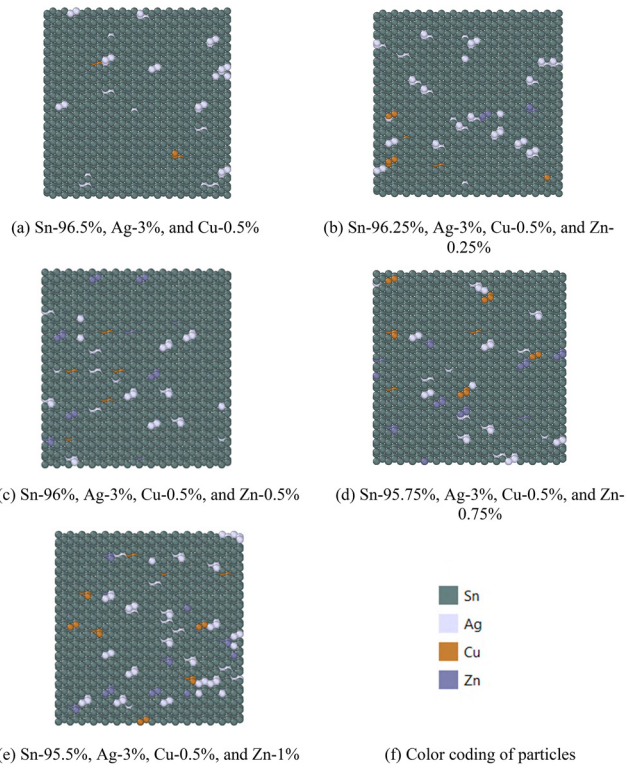

Fig. 2 (a–e) Illustrations of the five solder alloys with their respective constituent percentages, and (f) color coding of constituents.

weights. This ensured that the final atomistic models reproduced the correct weight–percentage compositions. The calculated numbers of Ag, Cu, and Zn atoms were then substituted into the Sn lattice either randomly or in a cluster form, as described in Section 2.5.

2.4 MD Simulations

The molecular dynamics modeling for solder materials was executed using the LAMMPS[53] simulation package. Visualization of the simulation outputs was carried out *via* OVITO[54] for better analysis. To maintain both precision and computational speed, a fixed time step of 1 femtosecond (fs) was selected.

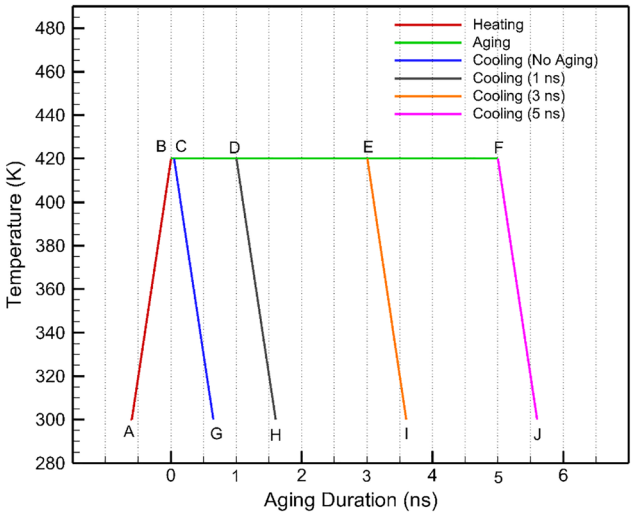

Fig. 3 Temperature variations during the heating, aging, and cooling phases of the structure.

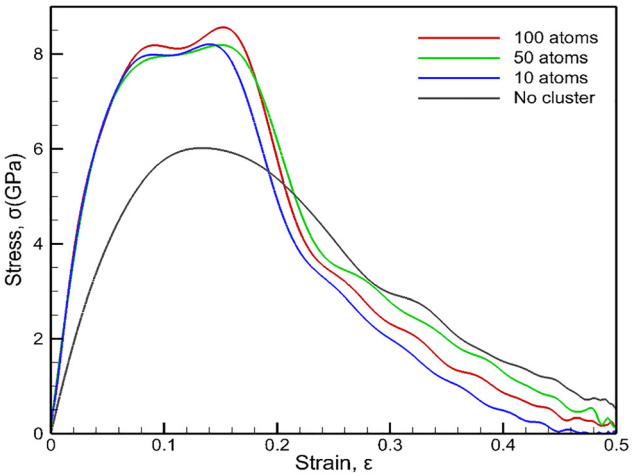

Fig. 4 Variations in stress with strain of SAC305 for different cluster sizes.

Initially, the energy was equilibrated (12.5 picoseconds (ps), NVE ensemble) using a Langevin thermostat. This step ensured thermal stability before proceeding to simulations conducted under an NPT ensemble, which utilized a Langevin thermostat to control the system's temperature and a Berendsen barostat to maintain the desired pressure. Following this, the system was switched back to the NPT ensemble for another 12.5 ps to stabilize before aging.

The heating process involved raising the temperature from 300 K to 420 K at a constant heating rate of 5 K ps^{-1} (A–B), followed by holding at 420 K for various durations, such as no aging (B–C), 1 ns (B–D), 3 ns (B–E) and 5 ns (B–F). After the holding phase, the system was then cooled to 300 K using a constant cooling rate of 5 K ps^{-1}. Fig. 3 illustrates the temperature variation throughout the heating, aging, and cooling phases.

After cooling, each simulation case was equilibrated at 300 K for 12.5 ps. Then, uniaxial tensile loading was applied along the x-direction under an NVT ensemble with a constant strain rate of 1×10^9 s^{-1}. In fracture-based loading, strain was applied until failure. The atomic-level stress was computed using the following virial expression:[55]

$$\sigma_{ij}^{\alpha} = \frac{1}{\Omega^{\alpha}}\left(\frac{1}{2}m^{\alpha}v_i^{\alpha}v_j^{\alpha} + \sum_{\beta=1,n} r_{\alpha\beta}^{j} f_{\alpha\beta}^{i}\right), \quad (2)$$

where i and j denote Cartesian components, m^{α} is the mass of the atom α, v^{α} is its velocity, $r_{\alpha\beta}^{j}$ is the displacement between the atoms α and β, and $f_{\alpha\beta}^{i}$ is the force exerted by atom β on atom α. Ω^{α} denotes the atomic volume of atom α.

2.5 Atomic clustering in SAC305 solder

To make the model of this study more physically realistic, a cluster-based substitution method was used instead of substituting single atoms. In actual materials, alloying elements tend to appear in clusters rather than as isolated atoms, and this approach better reflects how atoms behave in real-world alloys. Different cluster sizes of 1 (no cluster), 10, 50, and 100 atoms were examined to see how they impact stress–strain behavior. The results demonstrated that while clustering generally enhanced mechanical strength, cluster 100 exhibited instability beyond 0.15 strain, leading to abrupt stress fluctuations. Cluster 50, however, was the best option for the investigation of this study since it generated a stress–strain curve that was both physically precise and smooth. Hence, throughout this study, a random cluster size of 50 Sn atoms was used to replace Sn with Ag, Cu, and Zn.

It should be noted that the purpose of clustering in this study is not to model thermodynamic precipitates or fully equilibrated phases. Although real atomic agglomeration is influenced by Gibbs free-energy minimization, evaluating free energies for multiple cluster sizes in an 81 920-atom system is computationally impractical. Therefore, several cluster sizes (1, 10, 50, and 100 atoms) were assessed empirically, and the 50-atom cluster was selected because it produced stable, smooth stress–strain behavior (Fig. 4) without numerical artifacts. This makes cluster 50 a physically reasonable and mechanically reliable representation of localized alloying neighborhoods.

This methodology provides a more realistic representation of atomic-scale interactions and enhances the reliability of mechanical behavior predictions for SAC305 and Zn-doped SAC305 alloys.

3. Method validation

To ensure the reliability of the simulation methodology, two validation steps were performed: comparison of the stress–strain behavior and total energy–temperature trend in the solid phase during heating with the reference study.

3.1 DFT–MEAM lattice parameter validation

To validate the reliability of the MEAM potential for modeling Zn-doped Sn–Ag–Cu (SAC) alloys, we compared the equilibrium

lattice parameters predicted by molecular dynamics (MD) simulations with those obtained from first-principles density functional theory (DFT) calculations. Specifically, the Cu–Sn system was modeled using a hexagonal lattice; the Ag–Sn system was modeled using the orthorhombic Ag_3Sn phase; and the Zn–Sn system was modeled using the triclinic Zn_3Sn phase. The Cu–Zn system was modeled using an FCC structure, consistent with known β-brass data. These structures were used as the baseline to validate the MEAM-predicted lattice constants.

The DFT calculations were performed using the Quantum ESPRESSO package with the PBE exchange–correlation functional within the generalized gradient approximation (GGA). Ultrasoft pseudopotentials were employed, with plane-wave energy cutoffs of 60 Ry for the wave functions and 480 Ry for the charge density. A Monkhorst–Pack 8 × 8 × 8 *k*-point grid ensured total energy convergence within 1 meV per atom. Atomic relaxations were carried out using the BFGS algorithm until the forces on all atoms were less than 0.01 eV $Å^{-1}$. Spin polarization was not considered, as all systems are nonmagnetic.

In parallel, MD simulations were performed using the LAMMPS package with a multi-component MEAM potential. Elemental parameters for Sn, Ag, Cu, and Zn were taken from the literature. Each binary system was modeled in a 4 × 4 × 4 supercell and equilibrated under the NPT ensemble using a timestep of 1.0 fs. Temperature control was achieved using a Nosé–Hoover thermostat. The system was heated from 300 K to 600 K over 50 ps, equilibrated at 600 K for 100 ps, and cooled back to 300 K for lattice relaxation. The average lattice constants were extracted from the final 20 ps of the equilibrium trajectory.

Table 2 summarizes the comparison between the DFT and MEAM lattice parameters for representative binary alloys. MEAM systematically overestimates the DFT values by approximately 5–7%, which is consistent with the expected accuracy of semi-empirical interatomic potentials. For example, in the Cu–Sn hexagonal model, MEAM predicted a = 4.45 Å compared to the DFT value of a = 4.175 Å, a deviation of 6.6%. Similar deviations were found for the Ag–Sn and Zn–Sn systems, whereas Cu–Zn retained the DFT lattice constant value, showing excellent agreement. Despite small overestimations, the MEAM potential reproduces the relative trends and bonding characteristics observed in DFT, confirming its suitability for large-scale simulations of Zn-doped SAC alloys under flash-aging and thermal-cycling conditions.

Table 2 Comparison of equilibrium lattice parameters (*a*, *b*, and *c*) between DFT and MEAM for binary systems

Binary system	Lattice type	Parameter	DFT (Å)	MEAM (Å)	% Change
Cu–Sn	Hexagonal	$a = b$	4.175	4.450	6.59%
		c	5.097	5.420	6.34%
Ag–Sn	Orthorhombic	a	4.929	5.230	6.11%
		b	5.300	5.630	6.23%
		c	5.978	6.360	6.39%
Zn–Sn	Triclinic	a	4.524	4.800	6.10%
		b	5.834	6.190	6.10%
		c	6.757	7.210	6.70%
Cu–Zn	FCC	a	2.890	2.950	2.08%

3.2 Comparison of stress–strain behavior

To validate the simulation results, the stress–strain response of SAC305 under the No clustering and no-aging conditions was compared with a reference study[56] that used a similar SAC305 model subjected to heating and cooling at a rate of 10 K ps^{-1}.

The comparison depicted in Fig. 5 shows a close agreement in the overall curve shape and mechanical behavior. In this study, UTS was found to be 6.017 GPa, while the reference study obtained a UTS of 6.491 GPa, indicating strong consistency

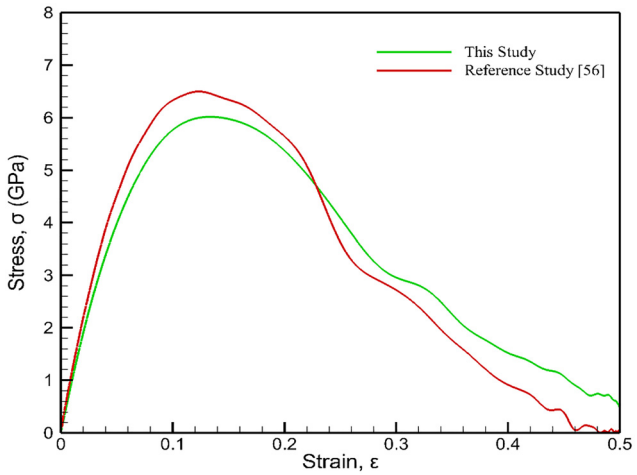

Fig. 5 Variations in stress–strain of SAC305 without clustering under the no-aging conditions.

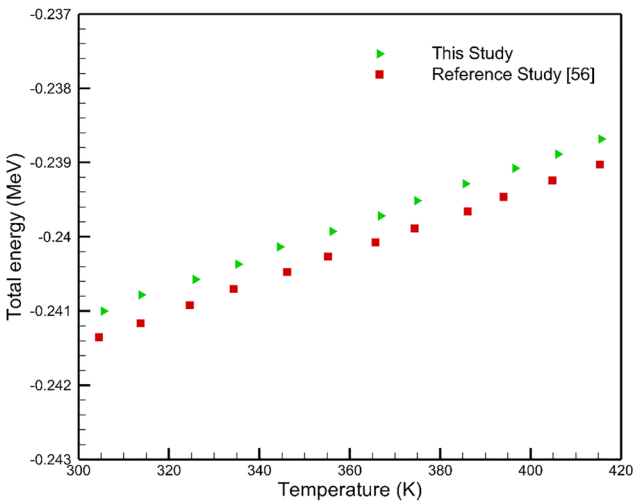

Fig. 6 Variations in the total energy of SAC305 with temperature during heating.

Table 3 Comparison of total energy at different temperatures

	Total energy (MeV)		
Temperature (K)	This study	Reference study[56]	Deviation (%)
305	−0.2410	−0.2413	0.124%
375	−0.2395	−0.2398	0.125%
415	−0.2386	−0.2390	0.168%

between both models and confirming the reliability of the simulation setup.

3.3 Comparison of total energy–temperature trend

The total energy was plotted against temperature, as shown in Fig. 6, for the No clustering SAC305 model compared with the reference study.[56] This study covers the heating of the solid-phase region over temperatures ranging from 305 K to 415 K, where the total energy increases linearly with temperature.

3.2.1 Slope comparison. In this study, the slope of the total energy curve is calculated as follows:

$$\frac{dE}{dT} = \frac{(-0.2386 + 0.2410) \times 10^6}{415 - 305} = 21.82 \text{ eV K}^{-1}.$$

The ref. 56 study shows a similar solid-phase slope (20.91 eV K^{-1}), confirming the accuracy of the results of this study.

3.2.2 Total energy comparison. At key temperature points, the total energy values of this study were closely matched with the reference study shown in Table 3.

Hence, the simulation of this study accurately reproduces the solid-phase behavior of SAC305. The calculated slope (21.82 eV K^{-1}) aligns with reference values (20.91 eV K^{-1}), and the total energy deviations are minimal (<0.2%), verifying model accuracy. These results verify the accuracy of the model used in this study in MD simulations.

4. Results and discussion

The effects of isothermal flash aging on the mechanical behavior of SAC305 solder alloys doped with different percentages of Zn are analyzed. Initially, the impact of isothermal aging on the uniaxial tensile test is observed, with a focus on key mechanical properties, such as UTS, YM, and energy absorption capacity up to UTS. Additionally, structural changes induced by isothermal aging are examined, particularly in terms of variations in the average atomic volume (AV) and RDF.

4.1 Impacts of flash aging on uniaxial stress–strain behavior

This section examines how flash aging affects the mechanical behavior of SAC305 solder alloys doped with different

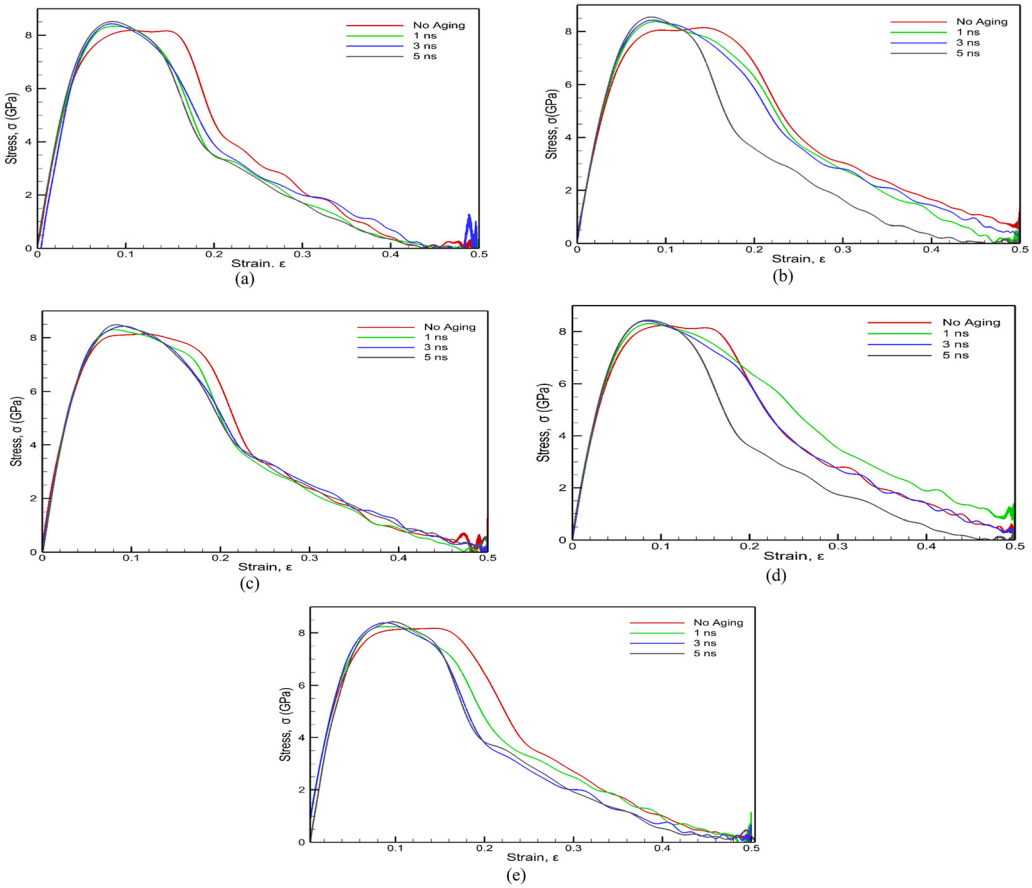

Fig. 7 Variations in stress with strain of (a) SAC305 and SAC305 doped with (b) 0.25%, (c) 0.5%, (d) 0.75%, and (e) 1% Zn.

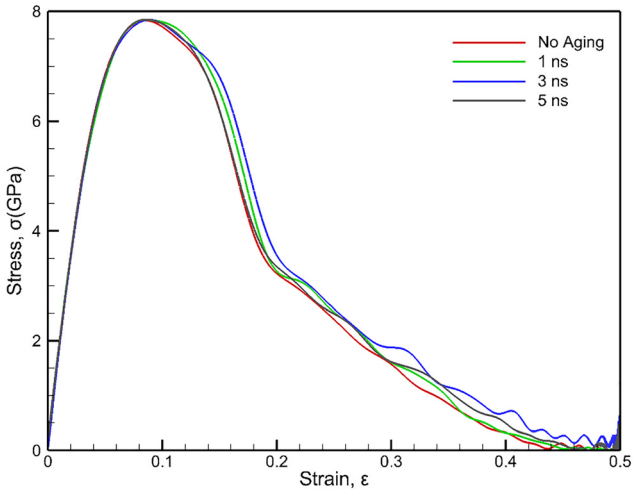

Fig. 8 Variations in stress with strain of SAC305 held at 300 K for different durations.

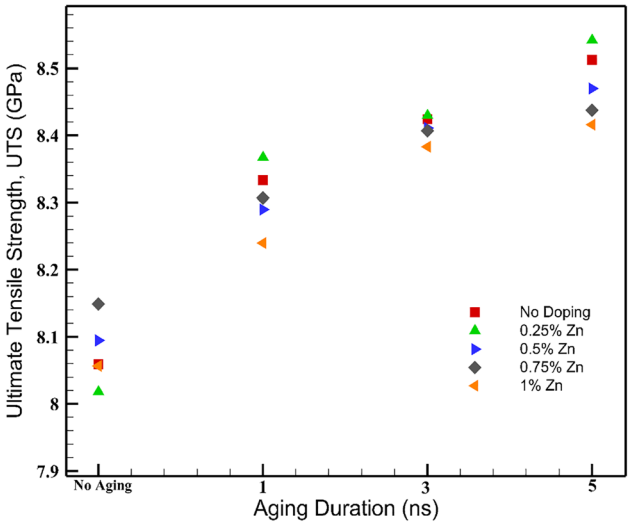

Fig. 9 Variations in UTS with aging for the SAC305 solder alloys doped with different percentages of Zn.

Table 4 UTS of SAC305 held at 300 K for different durations and their percentage change from the no-aging conditions

Aging durations (ns)	UTS (GPa)	% Change from 0 ns	% Change from 0 ns (at 420 k)
0	7.8302	N/A	N/A
1	7.8354	0.066	3.345
3	7.8399	0.124	5.294
5	7.8443	0.180	6.135

percentages of Zn under uniaxial tensile loading. The analysis is presented in two parts. First, the stress–strain response of each alloy is discussed to capture the overall mechanical behavior. To ensure that the observed changes in the stress–strain curves originate from the elevated-temperature flash-aging process rather than simply from longer simulation durations, an additional set of control simulations was performed at 300 K; these results are included after the main stress–strain analysis. Second, the variation in key mechanical properties, such as UTS, YM, and energy absorption capacity up to UTS, is explored with respect to both Zn doping concentrations and aging durations.

4.1.1 Stress–strain curve analysis. The stress–strain curves for SAC305 and SAC305 doped with varying percentages of Zn (0.25%, 0.5%, 0.75%, and 1%) at a constant strain rate of 1×10^9 s^{-1} are shown in Fig. 7(a)–(e) for different aging durations (no aging, 1 nanosecond (ns), 3 ns, and 5 ns).

The stress–strain responses differ noticeably. A significant change in mechanical properties is observed when the aging duration increases from no aging to 1 ns. However, for longer aging durations, such as 3 ns and 5 ns, stress–strain behavior remains relatively unchanged during the early stages of high-temperature aging. The doping of Zn slightly alters the stress–strain curve shape and peak stress values.

To verify that the observed differences in stress–strain behaviors are due to high-temperature-activated diffusion and structural relaxation occurring at 420 K and not simply a result of the longer simulation times, an additional set of control simulations was conducted at 300 K. These results are presented in the following subsection.

4.1.1.1 Control analysis at 300 K: aging time without heating. To isolate the effect of aging duration from temperature-driven aging, SAC305 was equilibrated at room temperature (300 K) for 12.5 ps and held at 300 K for different aging durations (no aging, 1 nanosecond (ns), 3 ns, and 5 ns). Subsequently, it was equilibrated again for 12.5 ps and then subjected to the same uniaxial tensile load. No heating to 420 K was performed in this control study. The stress–strain curves (Fig. 8) show almost complete overlap for all durations, demonstrating that the mechanical response remains unchanged even after several nanoseconds at room temperature.

As shown in Table 4, the UTS values vary by less than 0.2%, confirming that no meaningful densification, structural relaxation,

Table 5 UTS of SAC305 doped with different percentages of Zn

Aging durations (ns)	Ultimate tensile strength, UTS (GPa)				
	No doping (%increase)	0.25% Zn (%increase)	0.5% Zn (%increase)	0.75% Zn (%increase)	1% Zn (%increase)
0	8.059	8.018	8.095	8.149	8.057
1	8.333 (3.397)	8.367 (4.356)	8.290 (2.416)	8.307 (1.940)	8.240 (2.277)
3	8.424 (4.532)	8.430 (5.143)	8.411 (3.914)	8.407 (3.167)	8.383 (4.044)
5	8.512 (5.625)	8.542 (6.539)	8.470 (4.635)	8.438 (3.545)	8.416 (4.460)

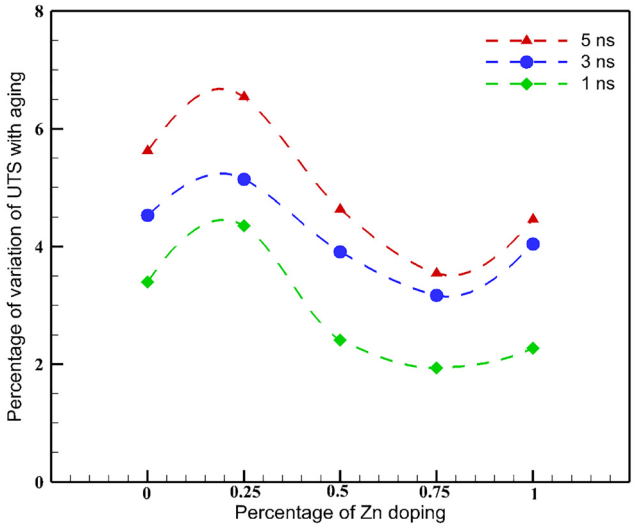

Fig. 10 Percentage variations in UTS under the no-aging condition across various aging durations for the SAC305 solder alloys doped with different percentages of Zn.

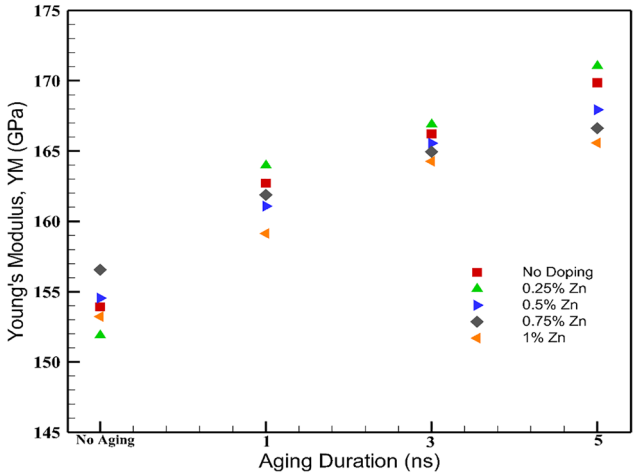

Fig. 11 Variations in YM with aging for the SAC305 solder alloys doped with different percentages of Zn.

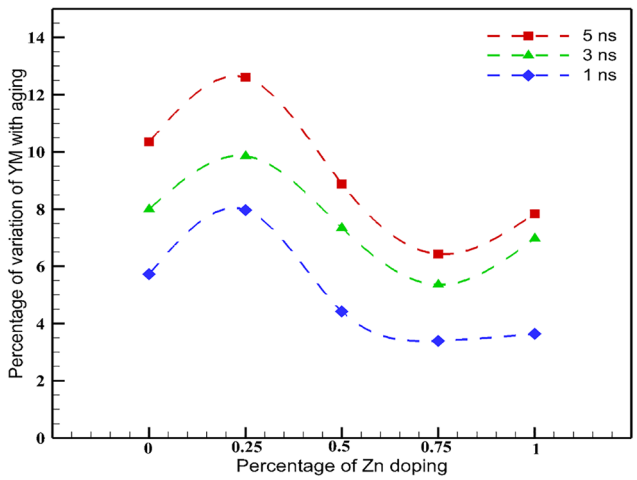

Fig. 12 Percentage variation in YM under the no-aging condition across various aging durations for SAC305 solder alloys doped with different percentages of Zn.

or strengthening occurs solely as a result of the simulation time at 300 K.

These findings verify that the mechanical behavior changes observed in the flash-aging simulations originate from the elevated-temperature aging process at 420 K and not from the total simulation duration at 300 K. The subsequent analysis in Section 4.1.2 depends on this result by quantifying these changes through UTS, YM, and energy absorption capacity metrics.

4.1.2 Variation of mechanical properties with zn doping and aging. The variation in UTS with aging duration for different Zn doping percentages is presented in Table 5 and Fig. 9 and 10. Across all compositions, UTS increases with longer aging durations, with the most significant increase occurring between no aging and 1 ns. The 0.25% Zn-doped SAC305 shows the highest overall increase (6.539%), followed by the undoped SAC305 (5.625%). In contrast, 0.75% Zn-doped SAC305 exhibits the smallest increase (3.545%), indicating better resistance to aging-induced UTS variation and more stable mechanical performance.

Young's modulus (YM) values for all compositions, shown in Table 6 and Fig. 11, 12, follow a trend similar to UTS. As the aging duration increases from 0 to 5 ns, YM increases in every case, with 0.25% Zn-doped SAC305 again showing the highest increase (12.607%). However, the 0.75% Zn-doped SAC305 exhibits a more moderate increase (6.431%), suggesting better mechanical consistency under thermal exposure. The results highlight that higher Zn doping helps reduce sensitivity to thermal aging in terms of stiffness.

Table 7 and Fig. 13, 14 show the variation in energy absorption capacity up to UTS with aging. The 0.25% Zn-doped SAC305 again displays the highest increase (9.106%), while the 0.75% Zn-doped alloy shows the lowest (4.025%) as the aging duration increases from 0 to 5 ns.

Table 6 YM of SAC305 doped with different percentages of Zn

Aging durations (ns)	Young's modulus, YM (GPa)				
	No doping (%increase)	0.25% Zn (%increase)	0.5% Zn (%increase)	0.75% Zn (%increase)	1% Zn (%increase)
0	153.922	151.909	154.251	156.574	153.547
1	162.724 (5.725)	163.986 (7.976)	161.086 (4.431)	161.883 (3.398)	159.140 (3.648)
3	166.221 (8.003)	166.920 (9.854)	165.570 (7.350)	164.959 (5.354)	164.277 (6.981)
5	169.851 (10.352)	171.057 (12.607)	167.945 (8.883)	166.635 (6.431)	556.825 (7.850)

Table 7 Energy absorption capacity up to UTS of SAC305 doped with different percentages of Zn

	Energy absorption capacity (GPa)				
Aging durations (ns)	No doping (%increase)	0.25% Zn (%increase)	0.5% Zn (%increase)	0.75% Zn (%increase)	1% Zn (%increase)
0	0.482	0.479	0.488	0.485	0.482
1	0.499 (3.345)	0.498 (4.120)	0.502 (2.869)	0.490 (1.092)	0.495 (2.727)
3	0.508 (5.294)	0.513 (7.192)	0.510 (4.508)	0.501 (3.298)	0.501 (3.837)
5	0.512 (6.135)	0.522 (9.106)	0.519 (6.352)	0.504 (4.025)	0.514 (6.445)

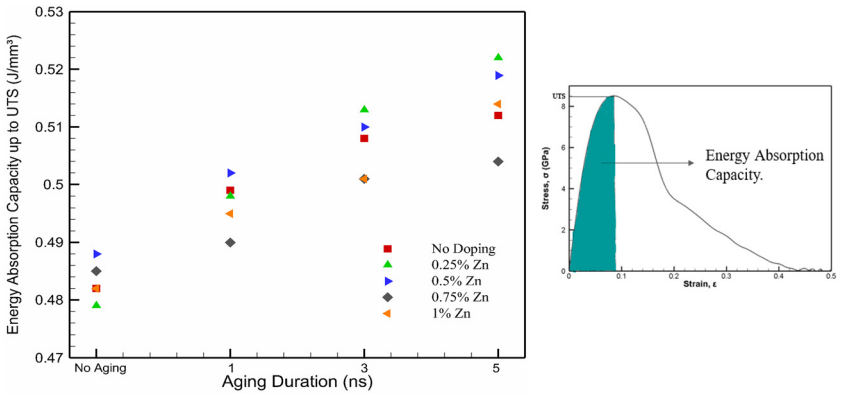

Fig. 13 Variations in the energy absorption capacity up to UTS with aging for the SAC305 solder alloys doped with different percentages of Zn.

These results clearly show that longer aging durations increase the mechanical properties, namely, UTS, YM, and energy absorption capacity, across all material compositions. Another notable observation is that the differences in these properties between 3 ns and 5 ns aging are quite small, indicating a saturation effect in mechanical property growth with prolonged aging.

In the case of SAC305, the rate of increase in UTS, YM, and energy absorption capacity with aging time durations is greater than that of Zn-doped SAC305 alloys, except for 0.25% Zn-doped SAC305. Although a higher absolute property value might be achieved in SAC305 with prolonged aging, the priority for reliable solder joints is mechanical stability, meaning minimal variation in properties over time. Furthermore, 0.75% Zn doping consistently demonstrates the smallest variations across all measured properties, indicating superior mechanical stability. These findings suggest that moderate Zn doping, especially at 0.75%, is optimal for minimizing the effects of flash aging and enhancing the reliability of lead-free solder joints.

4.2 Structural changes

The structural evolution of SAC305 and Zn-doped SAC305 alloys during aging was analyzed through necking behavior, variation in average atomic volume (AV), and RDF trends.

4.2.1 Influence of aging on necking. The tensile deformation analysis highlights a noticeable difference in necking

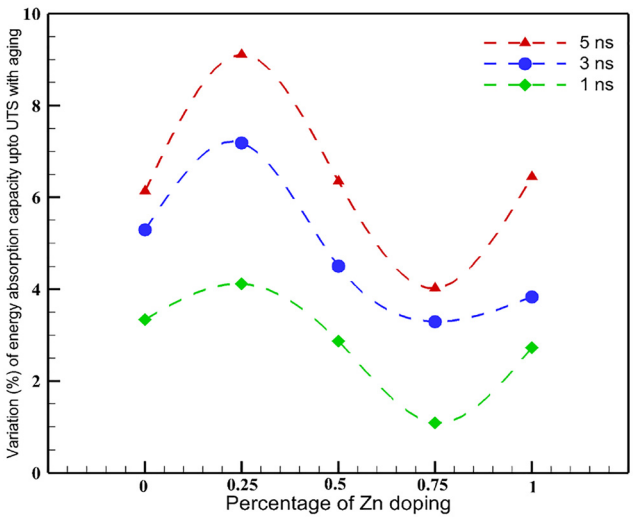

Fig. 14 Percentage variation in the energy absorption capacity up to UTS under the no-aging condition across various aging durations for the SAC305 solder alloys doped with different percentages of Zn.

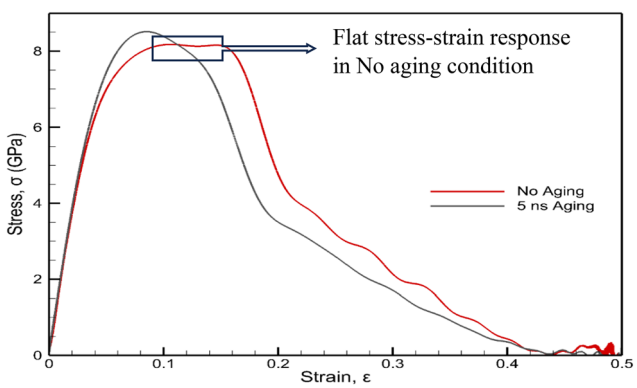

Fig. 15 Variations in stress with strain of SAC305 under the no-aging and 5-ns aging conditions.

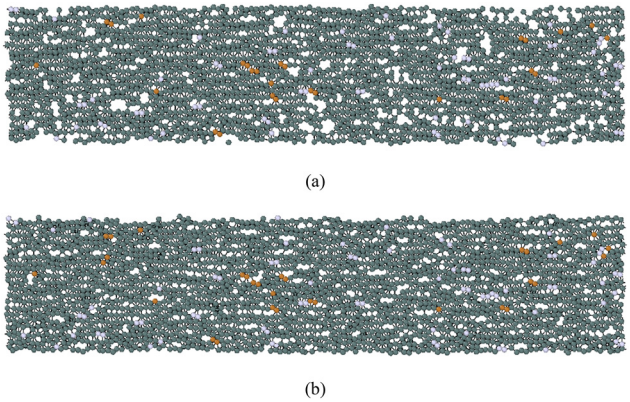

Fig. 16 Cross-sectional views of SAC305 during tensile test at 0.095 strain under the (a) no-aging and (b) 5-ns aging conditions.

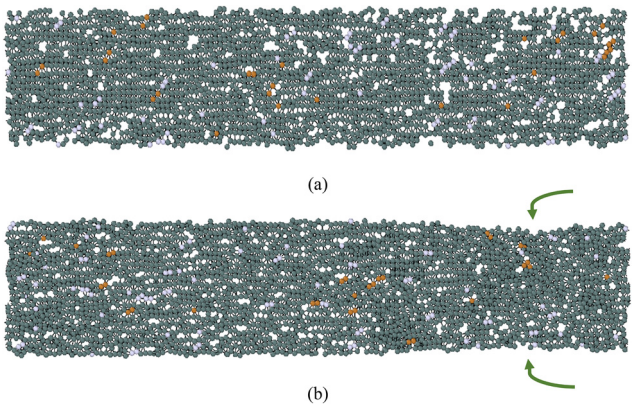

Fig. 17 Cross-sectional views of SAC305 during tensile test at 0.155 strain under the (a) no-aging and (b) 5-ns aging conditions.

behavior between unaged and aged (such as 5 ns) SAC305 samples, as shown in Fig. 15. At a strain of 0.095 (Fig. 16), both samples deform uniformly, showing no signs of necking. However, by the time strain reaches 0.155 (Fig. 17), the aged sample begins to show early necking somewhere within this range, and by 0.155 strain, some visible necking is already present. However, the unaged sample still holds uniform deformation throughout this interval, as reflected by the flat portion of its stress–strain curve between 0.095 and 0.155. By the time strain reaches 0.230 (Fig. 18), both samples display comparable levels of necking. These findings suggest that thermal aging primarily accelerates the onset of necking in SAC305 solder alloys although it does not significantly alter the eventual failure mechanism.

This early necking tendency in aged samples can be linked to structural densification caused by aging. As the average atomic volume decreases with aging, the material becomes more compact and, consequently, more brittle. This increase in brittleness makes the alloy more prone to localized deformation at an earlier stage. A detailed analysis of the average atomic volume and its variation across aging durations is presented in the next section.

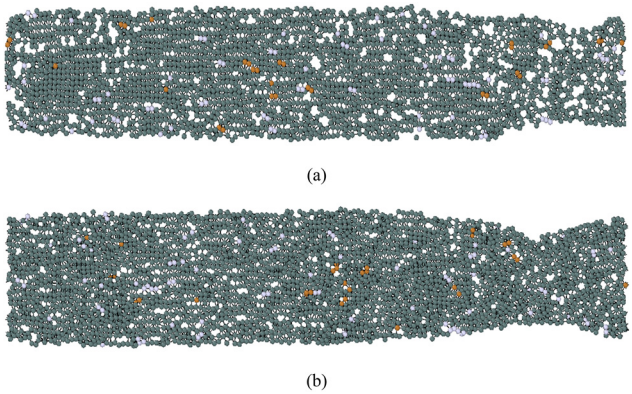

Fig. 18 Cross-sectional views of SAC305 during tensile test at 0.230 strain under the (a) no-aging and (b) 5-ns aging conditions.

4.2.2 Atomic volume (AV). In this study, the obtained results indicate a clear trend. As the aging duration increases, the average atomic volume of the material decreases, as illustrated in Fig. 19, signifying a densification process over time. For example, in SAC305, the atomic volume decreases from 573.785 to 557.102 cubic Å when the aging time is extended from no aging to 5 ns, yielding a reduction of 2.907%. Similar reductions are observed in the Zn-doped variants: the 0.25% Zn sample decreases from 575.830 to 557.940 cubic Å (3.107% reduction), the 0.5% Zn variant drops from 572.844 to 562.310 cubic Å (1.839%), the 0.75% Zn sample reduces from 571.395 to 563.197 cubic Å (1.435%), and the 1% Zn variant decreases from 570.933 to 556.825 cubic Å (2.471%). The decrease in

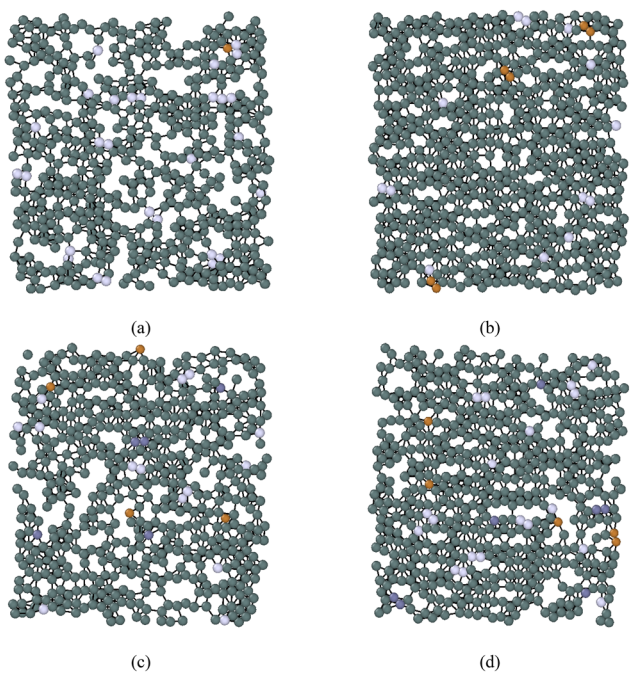

Fig. 19 Sample cross-sectional views before tensile test of SAC305 under the (a) no-aging and (b) 5-ns aging conditions, and 0.75% Zn doped SAC305 under the (c) no-aging and (d) 5-ns aging conditions.

Table 8 Average atomic volume of SAC305 doped with different percentages of Zn (before tensile loading)

Aging durations (ns)	Atomic volume, AV (Å^3)				
	No doping (%decrease)	0.25% Zn (%decrease)	0.5% Zn (%decrease)	0.75% Zn (%decrease)	1% Zn (%decrease)
0	573.785	575.830	572.844	571.395	570.933
1	565.867 (1.380)	566.540 (1.613)	565.406 (1.298)	565.974 (0.949)	563.418 (1.316)
3	559.304 (2.524)	560.296 (2.698)	563.055 (1.709)	564.817 (1.151)	559.282 (2.041)
5	557.102 (2.907)	557.940 (3.107)	562.310 (1.839)	563.197 (1.435)	556.825 (2.471)

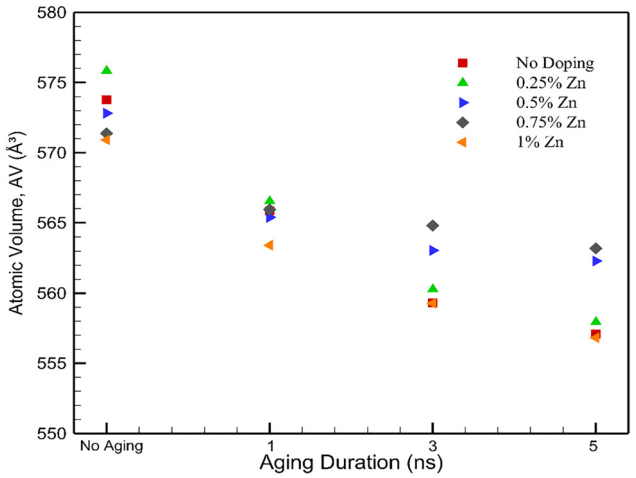

Fig. 20 Variations in average atomic volume (AV) with aging for the SAC305 solder alloys doped with different percentages of Zn.

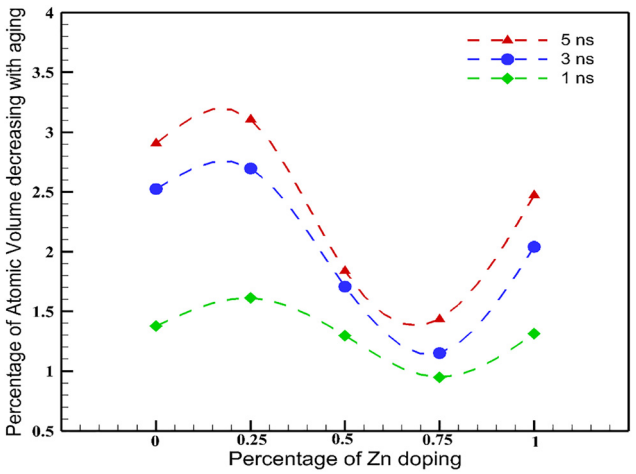

Fig. 21 Percentage reduction in average atomic volume under the no-aging condition across various aging durations for the SAC305 solder alloys doped with different percentages of Zn.

atomic volume across all compositions indicates general densification with aging.

In the case of SAC305, the rate of decrease in average atomic volume, or the rate of becoming denser with aging time durations, is higher compared to Zn-doped SAC305 alloys, except for 0.25% Zn-doped SAC305. Additionally, 0.75% Zn-doped SAC305 shows the lowest reduction rate in average atomic volume with aging time durations.

Table 8 and Fig. 20, 21 show the variation in the average atomic volume (AV) values with aging.

4.2.3 Radial distribution function (RDF). The variation in the RDF at different aging times for SAC305 and SAC305 doped with 0.25%, 0.5%, 0.75%, and 1% Zn is illustrated in Fig. 22. RDF analysis provides insights into structural changes, with peak height variations indicating structural relaxation. The RDF peak value change reflects the rate and magnitude of structural alteration, particularly in response to experimental conditions.[57,58]

Fig. 22(d) shows that as aging advances, the RDF peak values change at a slower rate than the others, suggesting that 0.75% Zn doping is ideal for reducing the impacts of aging on the mechanical characteristics of SAC305 at the nanoscale.

Although the absolute differences in the RDF peaks are small, such subtle variations are expected in amorphous or partially ordered metallic systems and still indicate measurable changes in the short-range atomic structure. As shown in the magnified inset of Fig. 22(b), the first-peak height decreases from approximately 300 at 3 ns to about 290 at 5 ns, representing nearly a 3% fluctuation. These modest but systematic shifts align with the observed densification during aging and provide supporting structural evidence for the mechanical property trends reported in this study.

5. Conclusions

This study examined the stress–strain behavior of lead-free solder alloys under uniaxial tensile loading in response to isothermal flash aging. The goal was to find the optimum amount of Zn doping to reduce the effects of aging on the alloy's strength. The main findings are as follows:

- A cluster of 50 atoms provides the most stable alloy's stress–strain behavior.
- The alloy's UTS, YM, and energy absorption up to UTS increased as it aged for a longer duration.
- Aging makes the alloy structure denser by reducing the average atomic volume (AV), which leads to increased UTS.
- The arrangement of atoms within the alloy changed noticeably as it aged, as shown by changes in the RDF.

This analysis demonstrated that UTS, YM, and energy absorption capacity up to UTS increased at a significant rate with aging time for the SAC305 structure at the nanoscale. However, the priority for reliable solder joints is mechanical stability, which minimizes variations in these properties across different aging durations. To minimize this undesirable trend, 0.25% Zn was added to SAC305, which led to a slight increase in the rate of UTS, YM, and energy absorption, contrary to the

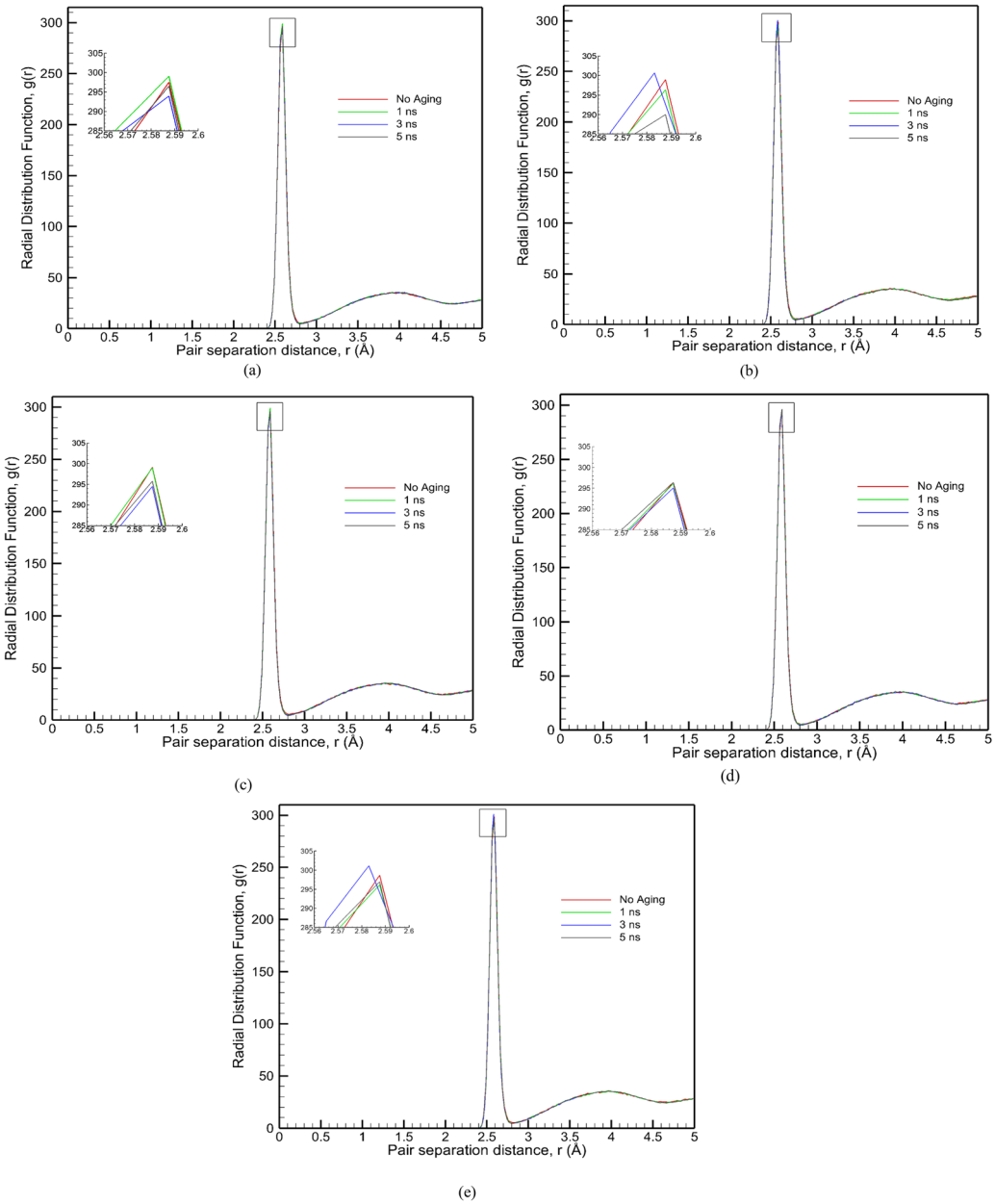

Fig. 22 Variation in RDF across different aging durations for (a) SAC305 and SAC305 doped with (b) 0.25%, (c) 0.5%, (d) 0.75%, and (e) 1% Zn. (For improved visibility, a magnified version of the peak region is plotted as an inset in the upper-left corner of each figure).

desired reduction. Subsequent tests with 0.5%, 0.75%, and 1% Zn doping showed that the rates of increase in UTS, YM, and energy absorption capacity were effectively reduced below those of SAC305. Out of all these compositions tested, SAC305 doped with 0.75% Zn showed the most consistent behavior under flash aging. It exhibited the smallest increase rate in UTS, YM, and energy absorption with aging. Additionally, this alloy showed the smallest decrease rate in average atomic volume (AV) and minimal changes in the RDF with aging.

These combined results suggest that 0.75% Zn doping is optimal for mitigating the effects of flash aging on the mechanical behavior of SAC305 at the nanoscale, offering a balance between structural stability and mechanical performance.

Author contributions

Md Nurul Islam and Ruman Ahmed Shijan: conceptualization, methodology, coding, visualization, formal analysis, data curation, writing – original draft. Mohammad Motalab: conceptualization, resources, writing – review and editing, supervision, funding acquisition. Md. Rafat Al Razy Rafi: methodology.

Conflicts of interest

The authors declare that they have no known competing financial or personal interests that could have influenced the results or interpretation of this work.

Data availability

Relevant data, models, or codes supporting the findings of this study can be made available by the corresponding author upon reasonable request.

Acknowledgements

We sincerely thank the Department of Mechanical Engineering and the Institute of Information and Communication Technology (IICT), BUET, for their support and facilities provided to conduct this research. We are also grateful to Mr. Md Habibur Rahman of Purdue University and Mr. Sadib Fardin of University of Maryland for their valuable contributions.

References

1 J. M. Davis, R. W. Elias and L. Grant, Current issues in human lead exposure and regulation of lead, *Neurotoxicology*, 1993, **14**(2–3), 15–27.
2 K. J. Puttlitz and K. A. Stalter, *Handbook of lead-free solder technology for microelectronic assemblies*. CRC Press, 2004.
3 O. Salmela, Acceleration factors for lead-free solder materials, *IEEE Trans. Compon., Packag. Technol.*, 2007, **30**(4), 700–707.
4 C. Wu, D. Q. Yu, C. Law and L. Wang, Properties of lead-free solder alloys with rare earth element additions, *Mater. Sci. Eng., R*, 2004, **44**(1), 1–44.
5 H. R. Kotadia, P. D. Howes and S. H. Mannan, A review: on the development of low melting temperature Pb-free solders, *Microelectron. Reliab.*, 2014, **54**(6–7), 1253–1273.
6 E. E. Mhd Noor, N. F. Mhd Nasir and S. R. A. Idris, A review: lead free solder and its wettability properties, *Soldering Surf. Mount Technol.*, 2016, **28**(3), 125–132.
7 M. McCormack, S. Jin, G. Kammlott and H. Chen, New Pb-free solder alloy with superior mechanical properties, *Appl. Phys. Lett.*, 1993, **63**(1), 15–17.
8 A. Schubert, *et al.*, Thermo-mechanical properties and creep deformation of lead-containing and lead-free solders, in Proceedings International Symposium on Advanced Packaging Materials Processes, Properties and Interfaces (IEEE Cat. No. 01TH8562), 2001: IEEE, pp. 129–134.
9 Y. Li, K.-S. Moon and C. Wong, Electronics without lead, *Science*, 2005, **308**(5727), 1419–1420.
10 J. Glazer, Microstructure and mechanical properties of Pb-free solder alloys for low-cost electronic assembly: a review, *J. Electron. Mater.*, 1994, **23**, 693–700.
11 K. Suganuma, *Lead-free soldering in electronics: Science, technology, and environmental impact*, CRC Press, 2003.
12 M. Abtew and G. Selvaduray, Lead-free Solders in Microelectronics, *Mater. Sci. Eng., R*, 2000, **27**(5), 95–141, DOI: 10.1016/S0927-796X(00)00010-3.
13 S. Cheng, C.-M. Huang and M. Pecht, A review of lead-free solders for electronics applications, *Microelectron. Reliab.*, 2017, **75**, 77–95, DOI: 10.1016/j.microrel.2017.06.016.
14 S. K. Kang, P. Lauro, D. Y. Shih, D. W. Henderson and K. J. Puttlitz, Microstructure and mechanical properties of lead-free solders and solder joints used in microelectronic applications, *IBM J. Res. Dev.*, 2005, **49**(4.5), 607–620, DOI: 10.1147/rd.494.0607.
15 M. Abtew and G. Selvaduray, Lead-free solders in microelectronics, *Mater. Sci. Eng., R*, 2000, **27**(5–6), 95–141.
16 A. Kroupa, *et al.*, Current problems and possible solutions in high-temperature lead-free soldering, *J. Mater. Eng. Perform.*, 2012, **21**, 629–637.
17 D. Suraski and K. Seelig, The current status of lead-free solder alloys, *IEEE Trans. Electron. Packag. Manuf.*, 2001, **24**(4), 244–248.
18 O. R. Adetunji, R. A. Ashimolowo, P. O. Aiyedun, O. M. Adesusi, H. O. Adeyemi and O. R. Oloyede, Tensile, hardness and microstructural properties of Sn–Pb solder alloys, *Mater. Today: Proc.*, 2021, **44**, 321–325, DOI: 10.1016/j.matpr.2020.09.656.
19 X. Long, S. Wang, X. He and Y. Yao, Annealing optimization for tin–lead eutectic solder by constitutive experiment and simulation, *J. Mater. Res.*, 2017, **32**(16), 3089–3099, DOI: 10.1557/jmr.2017.166.
20 I. Shohji, T. Yoshida, T. Takahashi and S. Hioki, Tensile properties of Sn–Ag based lead-free solders and strain rate sensitivity, *Mater. Sci. Eng., A*, 2004, **366**(1), 50–55, DOI: 10.1016/j.msea.2003.09.057.
21 H. Y. Lu, H. Balkan and K. S. Ng, Microstructure evolution of the Sn–Ag–*y*% Cu interconnect, *Microelectron. Reliab.*, 2006, **46**(7), 1058–1070.
22 M. Aamir, R. Muhammad, N. Ahmed and K. Alam, Impact of Thermal Aging on Microstructure and Mechanical Properties of high Sn Content, Sn–Pb Solders'', Fourth International Conference on Aerospace Science & Engineering, Islamabad, Pakistan, Institute of Space Technology, 2015.
23 M. Aamir, R. Muhammad, N. Ahmed and M. Waqas, Impact of thermal aging on the intermetallic compound particle size and mechanical properties of lead free solder for Green Electronics, *Microelectron. Reliab.*, 2017, **78**, 311–318, DOI: 10.1016/j.microrel.2017.09.022.
24 K. Hamasha, M. M. Hamasha and S. Hamasha, Effect of thermal aging on the mechanical properties of SAC305, *Materials*, 2022, **15**(8), 2816, DOI: 10.3390/ma15082816.
25 N. Hamada, T. Uesugi, Y. Takigawa and K. Higashi, Effects of Zn addition and aging treatment on tensile properties of Sn–Ag–Cu alloys, *J. Alloys Compd.*, 2012, **527**, 226–232, DOI: 10.1016/j.jallcom.2012.03.008.
26 M. Sadiq, R. Pesci and M. Cherkaoui, Impact of Thermal Aging on the Microstructure Evolution and Mechanical Properties of Lanthanum-Doped Tin-Silver-Copper Lead-Free Solders, *J. Electron. Mater.*, 2013, **42**, 492–501, DOI: 10.1007/s11664-012-2351-8.
27 H. Y. Song, Q. S. Zhu, Z. G. Wang, J. K. Shang and M. Lu, Effects of Zn addition on microstructure and tensile properties of Sn–1Ag–0.5Cu alloy, *Mater. Sci. Eng., A*, 2010, **527**(6), 1343–1350, DOI: 10.1016/j.msea.2009.10.048.
28 H. Y. Song, Q. S. Zhu, Z. G. Wang, J. K. Shang and M. Lu, Effects of Zn addition on microstructure and tensile properties of Sn–1Ag–0.5Cu alloy, *Mater. Sci. Eng., A*, 2010, **527**(6), 1343–1350, DOI: 10.1016/j.msea.2009.10.048.

29 H. Kotadia, P. D. Howes, D. P. Weston and S. H. Mannan, Reactions of Sn–3.5Ag-based solders containing Zn and Al additions on Cu and Ni(P) substrates, *J. Electron. Mater.*, 2010, **39**(12), 2720–2731, DOI: 10.1007/s11664-010-1404-x.

30 Y. K. Jee, Y. H. Ko and J. Yu, Effect of Zn on the intermetallic formation and reliability of Sn–3.5Ag solder on a Cu pad, *J. Mater. Res.*, 2007, **22**(7), 1879–1887, DOI: 10.1557/jmr.2007.0234.

31 R. Mayappan, I. Yahya, N. A. A. Ghani and A. H. Hamid, The effect of adding Zn into the Sn–Ag–Cu solder on the intermetallic growth rate, *J. Mater. Sci.: Mater. Electron.*, 2014, **25**(7), 2913–2922, DOI: 10.1007/s10854-014-1959-2.

32 H. L. J. Pang, Y. P. Wang, X. Q. Shi and Z. P. Wang, Sensitivity study of temperature and strain rate dependent properties on solder joint fatigue life, in Proceedings of 2nd Electronics Packaging Technology Conference (Cat. No. 98EX235), 10-10 Dec. 1998 1998, pp. 184–189, DOI: 10.1109/EPTC.1998.755999.

33 M. M. Chowdhury, R. Chowdhury, S. Ahmed, A. Fahim, J. Suhling and P. Lall, Mechanical Characterization of Doped SAC Solder Materials at High Temperature, *15th IEEE Intersociety Conference on Thermal and Thermomechanical Phenomena in Electronic Systems (ITherm), Las Vegas, NV, USA*, 2016, 1202–1208, DOI: 10.1109/ITHERM.2016.7517684.

34 A. Mahata, M. A. Zaeem and M. I. Baskes, Understanding homogeneous nucleation in solidification of aluminum by molecular dynamics simulations, *Modell. Simul. Mater. Sci. Eng.*, 2018, **26**(2), 025007, DOI: 10.1088/1361-651X/aa9f36.

35 J. Li, *et al.*, Tuning the mechanical behavior of high-entropy alloys via controlling cooling rates, *Mater. Sci. Eng., A*, 2019, **760**, 359–365, DOI: 10.1016/j.msea.2019.06.017.

36 L. Zhang, *et al.*, Molecular dynamics simulation of the interfacial evolution and whisker growth of copper-tin coating under electrothermal coupling, *Comput. Mater. Sci.*, 2022, **202**, 110981, DOI: 10.1016/j.commatsci.2021.110981.

37 M. Motalab, R. Paul, S. Saha, S. Mojumder, M. Ahmed and J. Suhling, Atomistic analysis of the thermomechanical properties of Sn–Ag–Cu solder materials at the nanoscale with the MEAM potential, *J. Mol. Model.*, 2019, **25**, 59, DOI: 10.1007/s00894-019-3939-1.

38 C. Li, Z. Lin, C. Zhang, W. Lai, M. Hu, L. Li, Y. Zhang, L. Zuo and L. Chen, Effect of aging treatment on microstructure and properties of Al–Cu–Mg alloy, *J. Phys.: Conf. Ser.*, 2022, **2383**(1), 012137, DOI: 10.1088/1742-6596/2383/1/012137.

39 M. R. Chowdhury, S. Ahmed, A. Fahim, J. C. Suhling and P. Lall, Mechanical characterization of doped SAC solder materials at high temperature, in 2016 15th IEEE Intersociety Conference on Thermal and Thermomechanical Phenomena in Electronic Systems (ITherm), 31 May-3 June 2016 2016, pp. 1202–1208, , DOI: 10.1109/ITHERM.2016.7517684.

40 Y.-C. Liu, W.-W. Wang, F. R. Jia, Z.-H. Zhu and X. Long, Temperature Effect on Tensile Behaviour of Sn–Pb Eutectic Solder, *International Conference on Computational, Modeling, Simulation and Mathematical Statistics (CMSMS 2018)*, 2018, DOI: 10.12783/dtcse/cmsms2018/25228.

41 M. I. Baskes, Modified embedded-atom potentials for cubic materials and impurities, *Phys. Rev. B: Condens. Matter Mater. Phys.*, 1992, **46**(5), 2727–2742, DOI: 10.1103/PhysRevB.46.2727.

42 M. I. Baskes, J. S. Nelson and A. F. Wright, Semiempirical modified embedded-atom potentials for silicon and germanium, *Phys. Rev. B: Condens. Matter Mater. Phys.*, 1989, **40**(9), 6085–6100, DOI: 10.1103/PhysRevB.40.6085.

43 M. I. Baskes and M. I. Baskes, Modified embedded-atom potentials for cubic materials and impurities, *Phys. Rev. B: Condens. Matter Mater. Phys.*, 1992, **46**(5), 2727–2742.

44 H. Fei, K. Yazzie, J. Williams and H. Jiang, Multiscale Modeling of the Interfacial Fracture Behavior in the Sn–Cu6 Sn5–Cu System, *J. Comput. Theor. Nanosci.*, 2011, **8**, 873–880, DOI: 10.1166/jctn.2011.1767.

45 H. Dong, L. Fan, K.-S. Moon, C. P. Wong and M. I. Baskes, MEAM molecular dynamics study of lead free solder for electronic packaging applications, *Modell. Simul. Mater. Sci. Eng.*, 2005, **13**(8), 1279, DOI: 10.1088/0965-0393/13/8/006.

46 R. Ravelo and M. Baskes, Equilibrium and Thermodynamic Properties of Grey, White, and Liquid Tin, *Phys. Rev. Lett.*, 1997, **79**(13), 2482–2485, DOI: 10.1103/PhysRevLett.79.2482.

47 B.-J. Lee, J.-H. Shim and M. I. Baskes, Semiempirical atomic potentials for the fcc metals Cu, Ag, Au, Ni, Pd, Pt, Al, and Pb based on first and second nearest-neighbor modified embedded atom method, *Phys. Rev. B: Condens. Matter Mater. Phys.*, 2003, **68**(14), 144112, DOI: 10.1103/PhysRevB.68.144112.

48 S. A. Etesami, M. I. Baskes, M. Laradji and E. Asadi, Thermodynamics of solid Sn and PbSn liquid mixtures using molecular dynamics simulations, *Acta Mater.*, 2018, **161**, 320–330, DOI: 10.1016/j.actamat.2018.09.036.

49 H.-S. Jang, K.-M. Kim and B.-J. Lee, Modified embedded-atom method interatomic potentials for pure Zn and Mg–Zn binary system, *Calphad*, 2018, **60**, 200–207, DOI: 10.1016/j.calphad.2018.01.003.

50 P. Hirel, Atomsk: a tool for manipulating and converting atomic data files, *Comput. Phys. Commun.*, 2015, **197**, 212–219, DOI: 10.1016/j.cpc.2015.07.012.

51 Python Software Foundation, *Python Language Reference (Version 3.11)*, 2023, https://www.python.org.

52 A. Hjorth Larsen, J. J. Mortensen, J. Blomqvist, I. E. Castelli, R. Christensen and M. Dułak, *et al.*, The Atomic Simulation Environment – a Python library for working with atoms, *J. Phys.: Condens. Matter*, 2017, **29**(27), 273002, DOI: 10.1088/1361-648X/aa680e.

53 S. Plimpton, Fast Parallel Algorithms for Short-Range Molecular Dynamics, *J. Comput. Phys.*, 1995, **117**(1), 1–19, DOI: 10.1006/jcph.1995.1039.

54 A. Stukowski, Visualization and analysis of atomistic simulation data with OVITO–the Open Visualization Tool, *Modell. Simul. Mater. Sci. Eng.*, 2010, **18**(1), 015012, DOI: 10.1088/0965-0393/18/1/015012.

55 M. Zhou, A new look at the atomic level virial stress: on continuum-molecular system equivalence, *Proc. R. Soc. London, Ser. A*, 2003, **459**(2037), 2347–2392, DOI: 10.1098/rspa.2003.1127.

56 S. Fardin, M. J. Moresalein, M. Motalab, A. Faiyad and R. Paul, Effects of ultra-high cooling rates on the tensile and cyclic stress–strain behavior of nanoscale solder materials, *J. Electron. Mater.*, 2025, **54**, 6828–6846, DOI: 10.1007/s11664-025-12048-6.

57 D. J. Srolovitz, T. Egami and V. Vitek, Radial Distribution Function and Structural Relaxation in Amorphous Solids, *Phys. Rev. B: Condens. Matter Mater. Phys.*, 1981, **24**(12), 6936–6944, DOI: 10.1103/PhysRevB.24.6936.

58 J. Li, H. Chen, S. Li, Q. Fang, Y. Liu, L. Liang, H. Wu and P. K. Liaw, Tuning the mechanical behavior of high-entropy alloys via controlling cooling rates, *Mater. Sci. Eng., A*, 2019, **760**, 359–365, DOI: 10.1016/j.msea.2019.06.022.